Frontiers of Physics
https://doi.org/10.1007/s11467-020-1017-x
Front. Phys.
16(3), 32502 (2021)

RESEARCH ARTICLE

Extracting the phase distribution of the electron wave packet ionized by an elliptically polarized laser pulse

Ya-Nan Qin[1], Min Li[1,†], Yudi Feng[1], Siqiang Luo[1], Yueming Zhou[1], Peixiang Lu[1,2,‡]

[1] *Wuhan National Laboratory for Optoelectronics and School of Physics, Huazhong University of Science and Technology, Wuhan 430074, China*
[2] *Hubei Key Laboratory of Optical Information and Pattern Recognition, Wuhan Institute of Technology, Wuhan 430205, China*
Corresponding authors. E-mail: †mli@hust.edu.cn, ‡lupeixiang@hust.edu.cn
Received July 28, 2020; accepted October 9, 2020

We use an interferometic scheme to extract the phase distribution of the electron wave packet from above-threshold ionization in elliptically polarized laser fields. In this scheme, an electron wave packet released from a circularly polarized laser pulse acts as a reference wave and interferes with the electron wave packet ionized by a time-delayed counter-rotating elliptically polarized laser field. The generated vortex-shaped interference pattern in the photoelectron momentum distribution enables us to extract the phase distribution of the electron wave packet in the elliptically polarized laser pulse with high precision. By artificially screening the ionic potential at different ranges when solving the time-dependent Schördinger equation, we find that the angle-dependent phase distribution of the electron wave packet in the elliptically polarized laser field shows an obvious angular shift as compared to the strong-field approximation, whose value is the same as the attoclock shift. We also show that the amplitude of the angle-dependent phase distribution is sensitive to the ellipticity of the laser pulse, providing an alternative way to precisely calibrate the laser ellipticity in the attoclock measurement.

Keywords above-threshold ionization, photoelectron interference, vortex structure

1 Introduction

The ionization of atoms and molecules in strong laser pulses can trigger a variety of strong field phenomena, such as high-order above-threshold ionization [1, 2], high-order harmonic and attosecond pulse generation [3, 4], and nonsequential double ionization [5, 6]. Compared with a linearly polarized laser pulse, there is an additional transverse electric field component for an elliptically polarized laser field, which suppresses the rescattering of the ionized electron with its parent ion. The resulting strong field phenomena are dramatically different from those in linearly polarized laser fields [7–11]. Therefore, the ionization in elliptically polarized laser fields has attracted much interest in recent years, and it has been shown to be important for the attoclock principle [12, 13], which is a powerful scheme to resolve attosecond electron dynamics in atoms and molecules. In the attoclock method [14, 15], precisely calibrating the ellipticity is a difficult task in the experiment [16]. Moreover, most of previous attoclock studies focused on the ionization rate of the electron wave packet (WP) in elliptically polarized laser fields [13, 17–19] and its phase distribution was ignored. The phase distribution of the electron WP [classical action of the strong-field approximation (SFA), which is a function of the electron momentum] is the key to understand the wavelike property of the electron [20] and thus it is the basis for matter wave interferometry. As far as we know, the phase distribution of the electron WP was only studied in circularly polarized laser fields [21, 22], and was not studied in elliptically polarized laser fields before.

In this work, we use an interferometic scheme to extract the phase distribution of the electron WP from above-threshold ionization (ATI) in an elliptically polarized laser field. We use another electron WP released from a circularly polarized laser field as a reference wave to interfere with the electron WP ionized by the elliptically polarized laser field, generating a photoelectron vortex structure in the photoelectron momentum distribution (PMD). Initially, this photoelectron vortex structure, an unusual kind of Ramsey interference [23] of laser induced electron WPs, was discovered and investigated in the single photon ionization by a pair of time-delayed counter-rotating circularly polarized laser pulses [24]. Subsequently, the vortex structures were studied in various processes, in-

*This article can also be found at http://journal.hep.com.cn/fop/EN/10.1007/s11467-020-1017-x.

cluding in multiphoton single ionization of He atoms [25], in single-photon double ionization of He [26] and H_2 [27], in two-color single ionization of molecular ions [28, 29], and in ionization of negative hydrogen ions [30]. Experimentally, spiral vortices were confirmed in the ionization of potassium atoms [21, 31] and sodium atoms [32]. Using the vortex-shaped momentum distribution, the electronic displacement in a ultrashort laser pulse was accurately extracted [22].

We find that, different from the vortex structure in a pair of circularly polarized laser pulses, the interference fringe of the vortex structure produced by a circularly polarized laser pulse and a time-delayed counter-rotating elliptically polarized laser pulse is unevenly spaced in the photoelectron angular distribution. From the modulation of the fringe spacing with the electron emission angle, we can extract the angle-dependent phase distribution of the electron WP in the elliptically polarized laser pulse with high precision. The results from the SFA are in a good agreement with the numerical solutions of the time-dependent Schördinger equation (TDSE) using a short-range potential. By artificially screening the ionic potential at different ranges when solving the TDSE, we find that the angle-dependent phase distribution in the elliptically polarized laser fields reveals a clear angular shift with respect to the SFA, whose value is the same as the attoclock shift. We further find that the amplitude of the angle-dependent phase distribution is sensitive to the laser ellipticity, which could be used to calibrate the pulse ellipticity with high precision.

2 Theoretical methods

2.1 SFA theory

In the SFA simulation, we use two time-delayed counter-rotating laser pulses to ionize a hydrogen atom, which consists of a left circularly polarized pulse (defined from the point of view of the receiver)

$$\boldsymbol{E}_1(t) = f(t)E_0[\cos(\omega t)\hat{\boldsymbol{e}}_x + \sin(\omega t)\hat{\boldsymbol{e}}_y], \tag{1}$$

and a time-delayed right elliptically polarized pulse

$$\begin{aligned}\boldsymbol{E}_2(t) =& f(t+\tau)\sqrt{\frac{2}{1+\varepsilon^2}}E_0\{\cos[\omega(t+\tau)]\hat{\boldsymbol{e}}_x \\ &- \varepsilon\sin[\omega(t+\tau)]\hat{\boldsymbol{e}}_y\}.\end{aligned} \tag{2}$$

where E_0 denotes the peak amplitude, ε is the ellipticity of the time-delayed elliptically polarized pulse, $\tau = 9T_0$ is the time delay between the two pulses, and ω is the angular frequency of the laser pulse ($\omega = 0.114$ a.u. corresponds to the laser wavelength of 400 nm). The laser pulse envelope $f(t) = \sin^2(\pi t/T_p)$ is employed with a duration of $T_p = 8T_0$, where T_0 is the period of the 400-nm laser field. We use atomic units (a.u.) throughout unless specified otherwise.

In the SFA, the transition amplitude from the ground state to the Volkov state with final momentum $\boldsymbol{p}$ is written as [33]

$$\begin{aligned}M_P =& -\mathrm{i}\int_{-\infty}^{\infty}\mathrm{d}t\exp[\mathrm{i}S(\boldsymbol{p},t)] \\ &\times\left[-\frac{2^{7/2}\times(2I_p)^{5/4}[\boldsymbol{p}+\boldsymbol{A}(t)]\cdot\boldsymbol{E}(t)}{\pi\{[\boldsymbol{p}+\boldsymbol{A}(t)]^2+2I_p\}^3}\right],\end{aligned} \tag{3}$$

where

$$S(\boldsymbol{p},t) = \int_{\infty}^{t}\mathrm{d}t'\frac{[\boldsymbol{p}+\boldsymbol{A}(t)]^2}{2} + I_p t \tag{4}$$

with I_p being the ionization potential of the hydrogen atom. In the simulation, Eq. (3) is directly integrated without relying on the saddle-point approximation.

The final doubly differential momentum distribution of the photoelectron is given by

$$\frac{\mathrm{d}^2P(p_x,p_y)}{\mathrm{d}p_x\mathrm{d}p_y} = |M_p|^2. \tag{5}$$

where p_x and p_y represent the final momenta along the x and y directions, respectively. The intensity of the laser field is set to be 3×10^{13} W/cm^2 in the simulation.

2.2 Numerical solutions of the TDSE

We also numerically solve the two-dimensional TDSE in the single-active-electron approximation. Using the length gauge, the TDSE can be written as

$$\mathrm{i}\frac{\partial}{\partial t}\Psi(\boldsymbol{r},t) = \left[-\frac{1}{2}\bigtriangledown^2 + V(r) + \boldsymbol{r}\cdot\boldsymbol{E}(t)\right]\Psi(\boldsymbol{r},t), \tag{6}$$

where $\Psi(\boldsymbol{r},t)$ is the electron wave function, $\boldsymbol{r} = (x,y)$ denotes the electron position, and $\boldsymbol{E}(t) = \boldsymbol{E}_1(t) + \boldsymbol{E}_2(t)$ is the electric field of the laser pulse.

In this paper, we use a soft-core Coulomb potential $V_l(r) = -\frac{1}{\sqrt{r^2+a}}$ and a short-range potential $V_s(r) = -\frac{1}{\sqrt{r^2+a}}\exp(-\frac{r^2}{b^2})$ in the TDSE calculation, with a being the soft parameter and b being the screening length of the short-range potential. As the screening length tends to infinity, the short-range potential becomes the Coulomb potential. For the case of the Coulomb potential, a is chosen to be 0.64 to match the ionization potential of the hydrogen atom. For the short-range potential, a is varied for different b to ensure the same binding energy for the Coulomb potential and short-range potential.

The split-operator spectral method is used on a Cartesian grid [34] ranges from -500 to 500 a.u. to numerically solve the two-dimensional TDSE. The time step is fixed at $\delta t = 0.1$ a.u. and the spatial discretization is $\delta x = \delta y = 0.2$ a.u.. The wave function in the whole two-dimensional space is divided into the inner wave function $\Psi_I(\tau)$ and the outer wave function $\Psi_{II}(\tau)$

smoothly by a splitting technique [35]. The wave function in the momentum space $C(\boldsymbol{p},\tau)$ is calculated by the Fourier transformation of the outer wave function. Finally, we obtain the final momentum distribution related to the sum of the wave function in the momentum space $\overline{C}(\boldsymbol{p},\tau) = \mathrm{e}^{-\mathrm{i}\int_{\tau}^{\infty}\frac{1}{2}[\boldsymbol{p}+\boldsymbol{A}(\tau')]^2\mathrm{d}\tau'}C(\boldsymbol{p},\tau)$ for each time step τ,

$$\frac{\partial^2 P(\boldsymbol{p})}{\partial F\partial\theta} = |\sum_{\tau}\overline{C}(\boldsymbol{p},\tau)|^2. \tag{7}$$

Here, F is electron energy associated with $\boldsymbol{p}$, θ is the angle of the emitted electron with respect to the x axis, and $A(\tau)$ is the vector potential of the laser field. The initial wave function is prepared by imaginary-time propagation [36].

3 Results and discussion

3.1 Extracting the phase distribution of the electron wave packet

We first show in Fig. 1(a) the PMD of the hydrogen atom in two time-delayed counter-rotating circularly polarized pulses calculated by the SFA. One can see many ring-like ATI structures centered at around zero momentum [marked by the white Arabic numerals in Fig. 1(a)], which come from the intercycle interference of the electron WPs [37, 38]. Notably, there is a left-helicity momentum vortex structure appearing within each ATI ring. From the view of multiphoton ionization, those electron vortex structures can be interpreted as a result of the interference of the free-electron WPs released by the two time-delayed laser pulses with different magnetic quantum numbers m [31]. In the left circularly polarized laser pulse, the phase distribution of the ionized electron WP as a function of the emission angle φ can be written as $g(\varphi) = +N\varphi$ ($-N\varphi$ for right circularly polarized laser pulse) [22], where φ is the electron emission angle with respect to the x axis [shown by the white arrow in Fig. 1(a)], and N is the number of photons absorbed by the atom for the corresponding ATI ring [i.e., $N\omega = I_p + p^2/2 + U_p$, where U_p is the ponderomotive potential, $U_p = (1+\varepsilon^2){E_0}^2/(4\omega^2)$]. Because the carrier frequency is 0.114 a.u. in our work, five photons are absorbed for the first order ATI. As shown in Fig. 1(a), there are ten spiral arms for the first order ATI ring in the PMD, which doubles the number of the photons absorbed in the ionization process [22, 24]. For the second-order ATI, the number of the spiral arms for the vortex structure is 12, which also doubles the number of the absorbed photons.

To study the phase distribution of the ionized electron WP in the elliptically polarized laser field, we take the electron WP released from a circularly polarized laser pulse as a reference, which interferes with the electron WP ionized by the time-delayed counter-rotating elliptically polarized laser pulse. The resulting PMD calculated by the SFA is shown in Fig. 1(b). Compared with Fig. 1(a), the ATI spectra show maximal ionization rate along the y axis (minor axis of the laser ellipse of the elliptically polarized laser pulse). There are also many vortex structures within each order ATI. The number of the spiral arms for the vortex structure within each order ATI is the same as that in Fig. 1(a). We next focus on the vortex structure within the first-order ATI ring. Figure 1(c) presents the photoelectron angular distribution within the first-order ATI ring at $p = 0.354$ a.u., as marked by a red-dashed circle in Fig. 1(b). Clearly, there is an oscillation with ten minima in the photoelectron angular distribution, which corresponds to five-photon absorption for the first order ATI ring. Thus, the angular difference $\Delta\varphi$ [shown by the red dash-dotted line in Fig. 1(c)] between two neighboring minima (adjacent angular fringe spacing) should be closed to $\pi/5$. However, a closer inspection reveals that the angular fringe spacing is larger around $\varphi = 0.5\pi$ than that around $\varphi = \pi$. The nonuniform spaced distribution means that the angle-dependent phase distribution in the elliptically polarized laser field does not linearly depend on φ.

Following the scheme described in Ref. [22], we can extract the angle-dependent phase distribution $g(\varphi)$ of the ionized electron WP from the nonuniform spaced vortex patterns. We denote the phase difference between the elliptically and circularly polarized laser fields as $f(\varphi) = g(\varphi) - N\varphi$, where $N\varphi$ is the angle-dependent phase distribution of the electron WP in a circularly polarized laser field. Because there is only a difference of $N\varphi$ between $g(\varphi)$ and $f(\varphi)$, $f(\varphi)$ is also referred to as the angle-dependent phase distribution in the following text. For circularly polarized laser field, $f(\varphi) = 0$. The phase difference for the vortex interference structure between $g_1(\varphi)$ and $g_2(\varphi)$ is given by $\Delta g(\varphi) = 2N\varphi + f(\varphi)$, where $g_1(\varphi)$ and $g_2(\varphi)$ represent the phase distribution of the electron WP ionized by the first and second laser pulses, respectively. In Fig. 1(c), the spacing of adjacent interference minima of the photoelectron angular distribution corresponding to a 2π value change. So the phase difference satisfies $|\Delta g_{k+1}(\varphi) - \Delta g_k(\varphi)| = 2\pi$, where the subscript k labels the number of the interference minimum in the photoelectron angular distribution. Therefore, the adjacent angular fringe spacing $\Delta\varphi$ can be expressed as

$$\Delta\varphi = \frac{2\pi - \Delta f(\varphi)}{2N}, \tag{8}$$

where $\Delta f(\varphi)$ is the phase difference of the electron WPs for adjacent interference minima. From the adjacent angular fringe spacing $\Delta\varphi$ in Fig. 1(c), we can obtain the phase distribution $f(\varphi)$ with respect to φ according to Eq. (8). Thus the angle-dependent phase distribution $f(\varphi)$ in the elliptically polarized laser field is directly obtained from the PMD. The extracted angle-dependent phase distribution from Figs. 1(a) and (b) are shown by the orange dotted line and the blue dashed line in

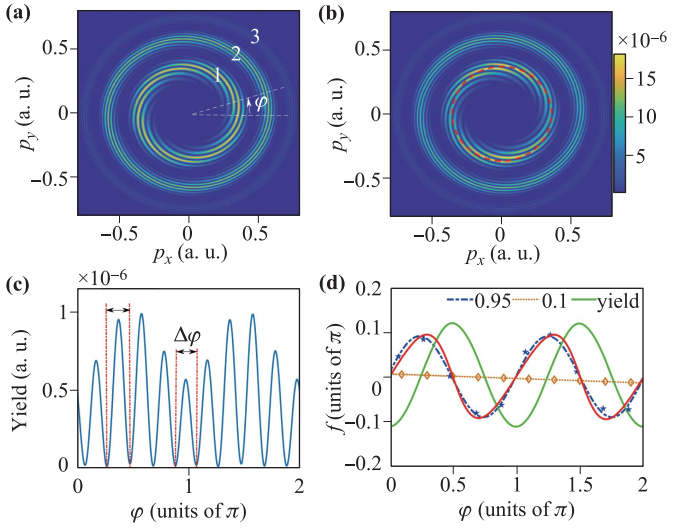

Fig. 1 **(a, b)** The PMDs in time-delayed counter-rotating laser pulses of (a) a pair of circularly polarized pulses and (b) a right circular pulse and a left elliptical pulse calculated by the SFA. The ellipticity of the elliptically polarized laser pulse is 0.95. p_x and p_y are the momenta along the major and minor axes of the laser ellipse, respectively. The color coding is on a logarithmic scale. **(c)** the photoelectron angular distribution within the first-order ATI ring at $p = 0.354$ a.u., as marked by red-dashed circle of (b). **(d)** the phase distribution of the electron WP (blue stars) as a function of the emission angle for the first-order ATI ring at $p = 0.354$ a.u. The blue dashed line is the fitting result of the blue stars. For comparison, we also show the electron yield of the first order ATI (integrated over a momentum range of 0.26 a.u.$< p <$0.44 a.u.) in the elliptically polarized laser field by the green solid line with arbitrary units.

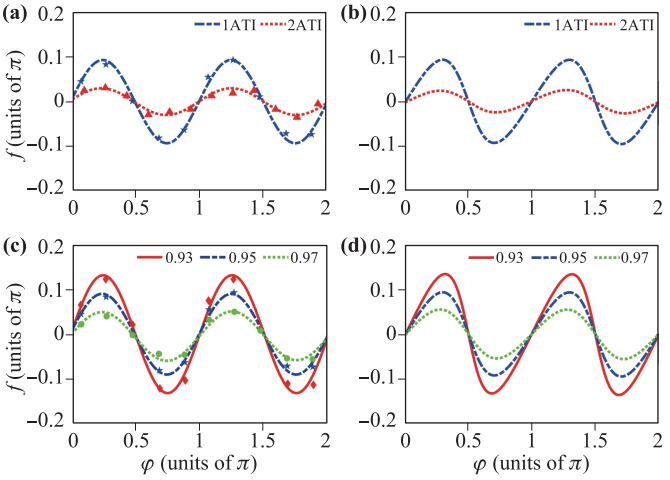

Fig. 2 The extracted angle-dependent phase distribution for different ATI orders **(a)** and different laser ellipticities **(c)** from the vortex-shaped momentum distribution calculated by the SFA. In (a), the blue dashed line and the red dotted line are the fitting of the stars and the triangles, respectively. In (c), the red solid line, the blue dashed line, and the green dotted line are the fitting of the rhombus, the stars, and the dots, respectively. For comparison, we also show the corresponding results in **(b)** and **(d)** from the transition amplitude of the SFA.

Fig. 1(d), respectively. In the SFA method, we can also obtain the angle-dependent phase distribution from the transition amplitude M_P [Eq. (3)] for a single elliptically polarized laser field. Note that in a real experiment, the transition amplitude in the SFA is not a direct observable. The angle-dependent phase distribution obtained from the transition amplitude of the SFA is shown by the red solid line in Fig. 1(d). One can see that the angle-dependent phase distribution extracted from the PMD agrees well with that obtained from the transition amplitude of a single elliptically polarized laser field. For comparison, in Fig. 1(d), we also show the electron yield of the first-order ATI (integrated over a momentum range of 0.26 a.u.$< p <$0.44 a.u.) in the elliptically polarized laser field by the green solid line with arbitrary units. It is interesting that the oscillation of the angle-dependent phase distribution show a clear phase shift of $\sim \pi/4$ with respect to the oscillation of the angle-dependent electron yield.

To validate our interferometic scheme, we compare the angle-dependent phase distributions extracted from the PMD and obtained from the transition amplitude for different orders of ATI and different laser ellipticities using the SFA method. In Fig. 2, the angle-dependent phase distributions in the left column are extracted from the PMD while in the right column are obtained from the transition amplitude of the SFA. Figures 2(a) and (b) present the angle-dependent phase distributions for the first-order and second-order ATI ring, which are denoted by the blue dash-dotted and red dotted curves, respectively. Clearly, the amplitude of the angle-dependent phase distribution decreases with the increase of the ATI order. In Figs. 2(c) and (d), the angle-dependent phase distributions in the elliptically polarized laser field with the ellipticities of 0.93, 0.95 and 0.97 are represented by the red solid, blue dash-dotted and green dotted curves, respectively. We find that, as the laser ellipticity increases, the amplitude of the angle-dependent phase distribution $f(\varphi)$ decreases, and tends to zero (the case of circular polarization). For different orders of ATI and different laser ellipticities, the angle-dependent phase distributions extracted from the vortex-shaped PMDs are in a good agreement with those obtained from the transition amplitude.

To interpret the angular phase shift between the oscillation of the photoelectron yield and the oscillation of angle-dependent phase distribution in Fig. 1(d), we express the phase distribution of the ionized electron WP in an elliptically polarized laser field by the quasiclassical action [39],

$$S = -\int_{t_0}^{\infty} \left(\frac{[\boldsymbol{p} + \boldsymbol{A}(t)]^2}{2} + I_p \right) \mathrm{d}t$$

$$= (I_p + \frac{p^2}{2} + U_p)t_0 + \frac{(\varepsilon^2 - 1){E_1}^2}{8\omega^3}\sin(2\omega t_0) + p_x\frac{E_1}{\omega^2}\cos(\omega t_0) + p_y\frac{\varepsilon E_1}{\omega^2}\sin(\omega t_0), \quad (9)$$

where t_0 is the ionization time of the electron. We take a half cycle of the laser field as an example. When $\omega t_0 = 0.5\pi$ (major axis of the laser ellipse), the phase distribution $S = (I_p + p^2/2 + U_p)t_0$ is the same as that of the circularly polarized laser field, i.e., the angle-dependent phase distribution $f(\varphi)$ is equal to zero, while the angle-dependent yield distribution reveals a maximum. When the phase distribution S is maximized, the ionization time obtained by solving Eq. (9) is around $\omega t_0 \approx 0.2\pi$. This means that there is an angular phase shift of $\sim \pi/4$ between the oscillation of the photoelectron yield and the oscillation of angle-dependent phase distribution, which is consistent with Fig. 1(d).

3.2 The effect of the ionic potential on the angle-dependent phase distribution

In shed light on the effect of the ionic potential on the phase distribution of the ionized electron wave packet, we show in Figs. 3(a) and (b) the vortex-shaped momentum distribution by solving the TDSE with the short-range potential ($b = 3$) and the Coulomb potential. As shown in Fig. 3(a), the result of the short range potential agrees well with the SFA. Compared with Fig. 3(a), the whole momentum spectra in Fig. 3(b) rotate counterclockwise under the influence of the Coulomb potential [40, 41]. Figure 3(c) shows the normalized electron yield of the first-order ATI (the data are integrated over a momentum range of 0.26 a.u.$< p <$0.44 a.u.) with respect to the angle φ for the Coulomb potential and the short-range potential. Obviously, with considering the effect of the Coulomb potential, the maximum of the electron yield exhibit a significant angular shift, i.e., attoclock shift [indicated by two dashed vertical lines in Fig. 3(c)], which is the main observable in the attoclock experiment [12, 13]. Figure 3(d) shows the photoelectron angular distribution within the first-order ATI ring at $p = 0.354$ a.u. for the Coulomb potential and the short-range potential with $b = 3$, which extracted from the vortex-shaped PMD of Figs. 2(a) and (b). From Fig. 3(d), one can see that the adjacent angular fringe spacing is changed under the influence of the Coulomb potential, which means that the ionic potential has a significant effect on the angle-dependent phase distribution in the elliptically polarized laser field. This is different from the case of circular polarization, in which the angle-dependent phase distribution is not influenced by the ionic potential due to the rotational symmetry of the laser field [22].

The extracted angle-dependent phase distributions for the first-order ATI ring at $p = 0.354$ a.u. from the vortex-shaped PMD are shown by the blue dotted lines in Fig. 4.

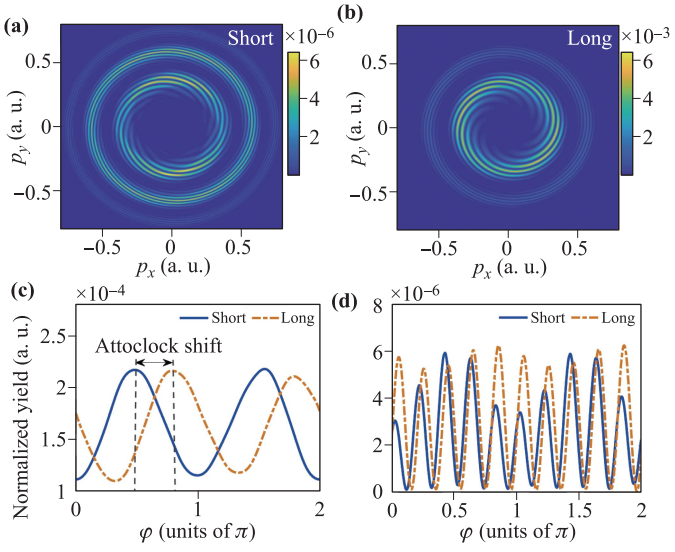

Fig. 3 **(a, b)** the vortex-shaped momentum distributions obtained by solving the TDSE for (a) a short-range potential with $b = 3$ and (b) the Coulomb potential. **(c)** the normalized yield of the first-order ATI with respect to the emission angle φ (integrated over a momentum range of 0.26 a.u.$< p <$0.44 a.u.). The attoclock shift is indicated by two dashed vertical lines. **(d)** the photoelectron angular distribution within the first-order ATI ring at $p = 0.354$ a.u. for the Coulomb potential (blue solid curve) and the short-range potential with $b = 3$ (yellow dashed curve).

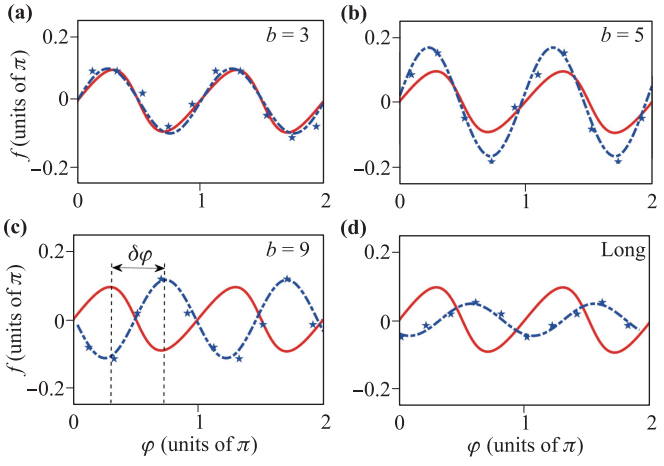

Fig. 4 The angle-dependent phase distribution for the first-order ATI ring at $p = 0.354$ a.u.. The blue stars represent the TDSE results extracted from the PMD in the time-delayed counter-rotating combined pulse of the circular and elliptical polarization, **(a–c)** the short-range potential with $b = 3$, 5, 9, respectively, and **(d)** the Coulomb potential. The blue dashed lines are the fitting results of the blue stars. The angular shift $\delta\varphi$ is indicated by two dashed vertical lines in Fig. 4(c). For comparison, the results of the SFA are shown by the red solid lines.

The PMD were obtained by solving the TDSE at different screening lengths. It is clear from Fig. 4 that there is an increasing angular shift for the angle-dependent phase distribution with the increase of the screening length. To quantitatively study this angular shift, we define $\delta\varphi$ as the angular shift [indicated by two dashed vertical lines in Fig. 4(c)] between the maxima of the angle-dependent phase distributions calculated by the TDSE (blue dashed lines) and the SFA (the red solid lines). The angular shift $\delta\varphi$ for the angle-dependent phase distribution with respect to the screening length b is shown by the blue solid circles in Fig. 5(a). One can see that the angular shift increases with the increase of the screening length. For comparison, we also show the attoclock shift for the first-order ATI as a function of the screening length b by the red solid line with triangles. One notices that the angular shift of the angle-dependent phase distribution is the same as the attoclock shift. Moreover, in Fig. 4, we can see that the amplitude of the angle-dependent phase distribution shows a dependence on the screening length. For $b = 3$ [Fig. 4(a)], The angle-dependent phase distribution calculated by the TDSE agrees with the SFA calculation. As can be seen from Figs. 4(b)–(d), the amplitude of the angle-dependent phase distribution [Figs. 4(b) and (c)] become larger for the screening lengths of 5 a.u. and 9 a.u., while it becomes smaller for the Coulomb potential [Fig. 4(d)] as compared to the SFA result. In Fig. 5(b), we show the amplitude of the angle-dependent phase distribution as a function of the screening length b for the ellipticity values of 0.91, 0.93, 0.95, and 0.97. One finds that the amplitude of the angle-dependent phase distribution first increases and then decreases with increasing the screening length of the ionic potential for all ellipticity values.

To qualitatively understand how the ionic potential influences the amplitude of angle-dependent phase distribution, we study the quasiclassical action along the electron trajectory. Without considering the effect of the ionic potential, the action of the electron WP can be expressed as $S = T + I_p t$, while with considering the effect of the ionic potential, the action is replaced by $S = T + V + I_p t$, where $V = \int_t^\infty \mathrm{d}\tau/|r(\tau)| \exp(-\frac{r(\tau)^2}{b^2})$ and $T = -\int_t^\infty \mathrm{d}\tau v^2/2$. The ionic potential affects both terms of V and T, and the contribution of V to the action S is opposite to that of T [42].

For the short-range potential with small value of b ($b = 3$), the effect of the ionic potential is ignored, so the amplitude of angle-dependent phase distribution is the same as the SFA calculation [Fig. 4(a)]. As the screening length increases, the predominant contribution (T or V) to the action S is changed, which might lead to the non-monotonic dependence of the amplitude on the screening length. Furthermore, in Fig. 5(b), though the ellipticity is slightly changed, the amplitude of the angle-dependent phase distribution has a considerable change for both short-range potential and Coulomb potential. This means the amplitude of the angle-dependent phase distribution depends sensitively on the laser ellipticity, which provides an alternative way to precisely calibrate the laser ellipticity in the attoclock measurement.

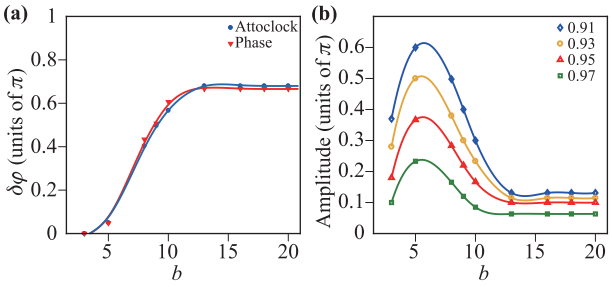

Fig. 5 **(a)** Comparison of the angular shift $\delta\varphi$ for the angle-dependent phase distribution (solid triangles) and the attoclock angular shift (solid circles) as a function of the screening length b, respectively. **(b)** The amplitude of $f(\varphi)$ as a function of b for different laser ellipticities, $\varepsilon = 0.91$ (hollow diamonds), 0.93 (hollow circles), 0.95 (hollow triangles), 0.97 (hollow squares).

4 Conclusion

In conclusion, we use an interferometic scheme to extract the phase distribution of the electron WP from the ATI in the elliptically polarized laser fields by modulating adjacent angular fringe spacing from the vortex-shaped photoelectron interference in the PMD. The results from the SFA are in a good agreement with the numerical solutions of the TDSE with a short range potential. Furthermore, we reveal the significance of the ionic potential on the angle-dependent phase distribution by artificially screening the ionic potential at different ranges. We find that the angle-dependent phase distribution shows an angular shift with respect to the SFA, and the value agrees well with the attoclock shift. Furthermore, the amplitude of the angle-dependent phase distribution is found to be sensitive to the ellipticity of the laser pulse. Our work provides a feasible tool for calibrating the ellipticity of the laser pulse and for understanding the wavelike property of the particle. Moreover, our results suggest that accurate descriptions of the strong-field ionization require complete characterization of both amplitude and phase of the continuum WP. This will impact the analysis of the time delay in strong-field ionization, which is believed to be closely related to the ionization phase. Looking ahead, because the ionization phase distribution is usually sensitive to the electron motion in atoms and molecules, accurate knowledge of the phase distribution of the continuum WP will pave the way to controlling the electron motion on the natural scale.

Acknowledgements This work was supported by the National Natural Science Foundation of China (Grants Nos. 11674116, 11722432, and 61475055).

References

1. G. G. Paulus, W. Nicklich, H. Xu, P. Lambropoulos, and H. Walther, Plateau in above threshold ionization spectra, *Phys. Rev. Lett.* 72(18), 2851 (1994)
2. H. Kang, W. Quan, Y. Wang, Z. Lin, M. Wu, H. Liu, X. Liu, B. B. Wang, H. J. Liu, Y. Q. Gu, X. Y. Jia, J. Liu, J. Chen, and Y. Cheng, Structure effects in angle-resolved high-order above-threshold ionization of molecules, *Phys. Rev. Lett.* 104(20), 203001 (2010)
3. J. L. Krause, K. J. Schafer, and K. C. Kulander, High-order harmonic generation from atoms and ions in the high intensity regime, *Phys. Rev. Lett.* 68(24), 3535 (1992)
4. F. Krausz and M. Ivanov, Attosecond physics, *Rev. Mod. Phys.* 81(1), 163 (2009)
5. B. Walker, B. Sheehy, L. F. DiMauro, P. Agostini, K. J. Schafer, and K. C. Kulander, Precision measurement of strong field double ionization of Helium, *Phys. Rev. Lett.* 73(9), 1227 (1994)
6. W. Becker, X. Liu, P. J. Ho, and J. H. Eberly, Theories of photoelectron correlation in laser-driven multiple atomic ionization, *Rev. Mod. Phys.* 84(3), 1011 (2012)
7. G. G. Paulus, F. Zacher, H. Walther, A. Lohr, W. Becker, and M. Kleber, Above-threshold ionization by an elliptically polarized field: Quantum tunneling interferences and classical dodging, *Phys. Rev. Lett.* 80(3), 484 (1998)
8. S. P. Goreslavski, G. G. Paulus, S. V. Popruzhenko, and N. I. Shvetsov-Shilovski, Coulomb asymmetry in above-threshold ionization, *Phys. Rev. Lett.* 93(23), 233002 (2004)
9. X. Wang and J. H. Eberly, Effects of elliptical polarization on strong-field short-pulse double ionization, *Phys. Rev. Lett.* 103(10), 103007 (2009)
10. C. Liu and K. Z. Hatsagortsyan, Coulomb focusing in above-threshold ionization in elliptically polarized mid-infrared strong laser fields, *Phys. Rev. A* 85(2), 023413 (2012)
11. C. Wang, X. Lai, Z. Hu, Y. Chen, W. Quan, H. Kang, C. Gong, and X. Liu, Strong-field atomic ionization in elliptically polarized laser fields, *Phys. Rev. A* 90(1), 013422 (2014)
12. P. Eckle, M. Smolarski, P. Schlup, J. Biegert, A. Staudte, M. Schöffler, H. G. Muller, R. Dörner, and U. Keller, Attosecond angular streaking, *Nat. Phys.* 4(7), 565 (2008)
13. P. Eckle, A. N. Pfeiffer, C. Cirelli, A. Staudte, R. Dörner, H. G. Muller, M. Büttiker, and U. Keller, Attosecond ionization and tunneling delay time measurements in helium, *Science* 322(5907), 1525 (2008)
14. J. Liang, Y. Zhou, J. Tan, M. He, Q. Ke, Y. Zhao, M. Li, W. Jiang, and P. Lu, Low-energy photoelectron interference structure in attosecond streaking, *Opt. Express* 27(26), 37736 (2019)
15. J. Yan, W. Xie, M. Li, K. Liu, S. Luo, C. Cao, K. Guo, W. Cao, P. Lan, Q. Zhang, Y. Zhou, and P. Lu, Photoelectron ionization time of aligned molecules clocked by attosecond angular streaking, *Phys. Rev. A* 102(1), 013117 (2020)
16. C. Wang, X. Li, X. Xiao, Y. Yang, S. Luo, X. Yu, X. Xu, L. Peng, Q. Gong, and D. Ding, Accurate in situ measurement of ellipticity based on subcycle ionization dynamics, *Phys. Rev. Lett.* 122(1), 013203 (2019)
17. I. A. Ivanov and A. S. Kheifets, Strong-field ionization of He by elliptically polarized light in attoclock configuration, *Phys. Rev. A* 89, 021402(R) (2014)
18. L. Torlina, F. Morales, J. Kaushal, I. Ivanov, A. Kheifets, A. Zielinski, A. Scrinzi, H. G. Muller, S. Sukiasyan, M. Ivanov, and O. Smirnova, Interpreting attoclock measurements of tunnelling times, *Nat. Phys.* 11(6), 503 (2015)
19. N. Camus, E. Yakaboylu, L. Fechner, M. Klaiber, M. Laux, Y. Mi, K. Z. Hatsagortsyan, T. Pfeifer, C. H. Keitel, and R. Moshammer, Experimental evidence for quantum tunneling time, *Phys. Rev. Lett.* 119(2), 023201 (2017)
20. K. Liu, M. Li, W. Xie, K. Guo, S. Luo, J. Yan, Y. Zhou, and P. Lu, Revealing the effect of atomic orbitals on the phase distribution of an ionizing electron wave packet with circularly polarized two-color laser fields, *Opt. Express* 28(8), 12439 (2020)
21. D. Pengel, S. Kerbstadt, D. Johannmeyer, L. Englert, T. Bayer, and M. Wollenhaupt, Electron vortices in femtosecond multiphoton ionization, *Phys. Rev. Lett.* 118(5), 053003 (2017)
22. X. Xiao, M. Wang, H. Liang, Q. Gong, and L. Peng, Proposal for measuring electron displacement induced by a short laser pulse, *Phys. Rev. Lett.* 122(5), 053201 (2019)
23. N. Ramsey, A molecular beam resonance method with separated oscillating fields, *Phys. Rev.* 78(6), 695 (1950)
24. J. M. Ngoko Djiokap, S. X. Hu, L. B. Madsen, N. L. Manakov, A. V. Meremianin, and A. F. Starace, Electron vortices in photoionization by circularly polarized attosecond pulses, *Phys. Rev. Lett.* 115(11), 113004 (2015)
25. J. M. Ngoko Djiokap, A. V. Meremianin, N. L. Manakov, S. X. Hu, L. B. Madsen, and A. F. Starace, Multistart spiral electron vortices in ionization by circularly polarized UV pulses, *Phys. Rev. A* 94(1), 013408 (2016)
26. J. M. Djiokap, A. V. Meremianin, N. L. Manakov, S. X. Hu, L. B. Madsen, and A. F. Starace, Kinematical vortices in double photoionization of helium by attosecond pulses, *Phys. Rev. A* 96(1), 013405 (2017)
27. J. M. Ngoko Djiokap, A. V. Meremianin, N. L. Manakov, L. B. Madsen, S. X. Hu, and A. F. Starace, Dynamical electron vortices in attosecond double photoionization of H_2, *Phys. Rev. A* 98(6), 063407 (2018)
28. K. J. Yuan, S. Chelkowski, and A. D. Bandrauk, Photoelectron momentum distributions of molecules in bichromatic circularly polarized attosecond UV laser fields, *Phys. Rev. A* 93(5), 053425 (2016)
29. K. J. Yuan, H. Lu, and A. D. Bandrauk, Photoionization of triatomic molecular ions H_3^{2+} by intense bichromatic circularly polarized attosecond UV laser pulses, *J. Phys. At. Mol. Opt. Phys.* 50(12), 124004 (2017)
30. J. Chen, X. Zheng, and T. Zhang, Vortex structures in the photoelectron momentum distributions of negative hydrogen ions induced by a short laser pulse, *Proc. SPIE* 11333, 46 (2019)

31. D. Pengel, S. Kerbstadt, L. Englert, T. Bayer, and M. Wollenhaupt, Control of three-dimensional electron vortices from femtosecond multiphoton ionization, *Phys. Rev. A* 96(4), 043426 (2017)
32. S. Kerbstadt, K. Eickhoff, T. Bayer, and M. Wollenhaupt, Odd electron wave packets from cycloidal ultrashort laser fields, *Nat. Commun.* 10(1), 658 (2019)
33. S. Yu, Y. Wang, X. Lai, Y. Huang, W. Quan, and X. Liu, Coulomb effect on photoelectron momentum distributions in orthogonal two-color laser fields, *Phys. Rev. A* 94(3), 033418 (2016)
34. M. D. Feit, J. A. Jr Fleck, and A. Steiger, Solution of the Schördinger equation by a spectral method, *J. Comput. Phys.* 47(3), 412 (1982)
35. X. M. Tong, K. Hino, and N. Toshima, Phase-dependent atomic ionization in few-cycle intense laser fields, *Phys. Rev. A* 74, 031405(R) (2006)
36. M. Protopapas, C. H. Keitel, and P. L. Knight, Atomic physics with super-high intensity lasers, *Rep. Prog. Phys.* 60(4), 389 (1997)
37. M. Li, J. W. Geng, H. Liu, Y. Deng, C. Wu, L. Y. Peng, Q. Gong, and Y. Liu, Classical-quantum correspondence for above-threshold ionization, *Phys. Rev. Lett.* 112(11), 113002 (2014)
38. H. Xie, M. Li, S. Luo, Y. Li, Y. Zhou, W. Cao, and P. Lu, Energy-dependent angular shifts in the photoelectron momentum distribution for atoms in elliptically polarized laser pulses, *Phys. Rev. A* 96(6), 063421 (2017)
39. M. Lewenstein, P. Balcou, M. Y. Ivanov, A. L'Huillier, and P. B. Corkum, Theory of high-harmonic generation by low-frequency laser fields, *Phys. Rev. A* 49(3), 2117 (1994)
40. M. Li, Y. Liu, H. Liu, Q. Ning, L. Fu, J. Liu, Y. Deng, C. Wu, L. Peng, and Q. Gong, Subcycle dynamics of Coulomb asymmetry in strong elliptical laser fields, *Phys. Rev. Lett.* 111(2), 023006 (2013)
41. A. S. Landsman, C. Hofmann, A. N. Pfeiffer, C. Cirelli, and U. Keller, Unified approach to probing Coulomb effects in tunnel ionization for any ellipticity of laser light, *Phys. Rev. Lett.* 111(26), 263001 (2013)
42. P. A. Korneev, S. V. Popruzhenko, S. P. Goreslavski, T. M. Yan, D. Bauer, W. Becker, M. Kübel, M. F. Kling, C. Rödel, M. Wünsche, and G. G. Paulus, Interference carpets in above-threshold ionization: From the Coulomb-free to the coulomb-dominated regime, *Phys. Rev. Lett.* 108(22), 223601 (2012)